Available online at www.sciencedirect.com
ScienceDirect
International Journal of Heat and Mass Transfer 50 (2007) 3498–3506
International Journal of HEAT and MASS TRANSFER
www.elsevier.com/locate/ijhmt

Vascularized materials with heating from one side and coolant forced from the other side

S. Kim [a], S. Lorente [b], A. Bejan [a,*]

[a] Department of Mechanical Engineering and Materials Science, Duke University, Durham, NC 27708-0300, USA
[b] Laboratoire Matériaux et Durabilité des Constructions, Département de Génie Civil, Institut National des Sciences Appliquées, 135 Avenue de Rangueil, 31077 Toulouse, France

Received 6 November 2006; received in revised form 6 January 2007
Available online 2 April 2007

Abstract

The vascularization of smart materials with the property of localized self-cooling is investigated here on the basis of a simple configuration. A solid body (slab) is subjected to intense heat flux from one side; temperatures are controlled by pumping a coolant from the other side. The coolant flows through parallel channels that traverse the slab. The objective is to find the channel configuration that maintains the least nonuniform temperature distribution in the solid (i.e., the coolest hot spots). The optimal spacing between channels and the minimum hot-spot excess temperature are deduced analytically for two configurations, equidistant parallel-plates channels, and arrays of equidistant parallel cylindrical channels. These analytical results are confirmed based on numerical simulations of the conjugate heat transfer in channels and surrounding solid material. The results for the optimal geometry and performance are robust: they are essentially the same for parallel-plates and cylindrical channels.

Keywords: Constructal theory; Vascularized materials; Smart materials; Self-cooling; Optimal spacings; Designed porous media

1. Vascularized smart materials

Engineering is witnessing a surge of interest in bio-inspired designs of flow architectures that promise superior properties, for example, volumetrically distributed and high-density heat and mass transfer. A stimulus for this new direction is the emergence of constructal theory [1] as a means to explain biological and geophysical design, and as a method for developing new concepts for engineered flow architectures. This new research direction was reviewed in Refs. [2,3], and is not reviewed again here (see also the last paragraph).

The new drive to discover novel flow architecture comes at a time when the development of smart materials is undergoing a vascularization revolution. Future smart materials promise entirely new functionality (e.g., self-healing, self-cooling [4–8]) which rests squarely on the ability to bathe on demand—at every point—solid bodies that perform more traditional functions (mechanical loading, sensing, actuating, morphing). Constructal theory [1,2] serves the vascularization needs of new smart structures ideally, because it frees the mind to discover the configuration, i.e. to morph the flow architecture in time in the direction of configurations that provide greater access.

In this paper we consider the challenge to vascularize a solid body with the ultimate objective of building into the body structure the function of self-cooling. The body may experience sudden or steady heating from one side. The need is to send a coolant to the heated spots fast, efficiently and reliably. For this the body design needs vascularization, which must carry the coolant from one entry point to the finite-size area that needs cooling.

In the present study we take the first step, the most fundamental, and model the whole problem on one axis (Fig. 1): the solid body is in the middle, the heat attack

* Corresponding author. Tel.: +1 919 660 5309; fax: +1 919 660 8963.
E-mail address: dalford@duke.edu (A. Bejan).

0017-9310/$ - see front matter © 2007 Elsevier Ltd. All rights reserved.
doi:10.1016/j.ijheatmasstransfer.2007.01.020

Nomenclature

a, b	exponents, Section 5
B	pressure drop number, Be, Eq. (18)
c_P	specific heat at constant pressure, J/kg K
D	channel thickness, m
g	function, $32/\phi$
H	spacing between channels, m
k	specific heat, W/m K
K	permeability, m^2
L	length, m
q''	heat flux, W/m^2
V	volume averaged velocity, m/s
T	temperature, K
x, y	cartesian coordinates, m

Greek symbols

α	thermal diffusivity of porous medium, Section 2.1
ΔT	temperature difference, K
ε	convergence criterion
μ	viscosity, kg/sm
ρ	density, kg/m^3
ϕ	volume fraction

Subscripts

f	fluid
max	maximum
min	minimum
opt	optimum
s	solid
x	measured along x
y	measured along y

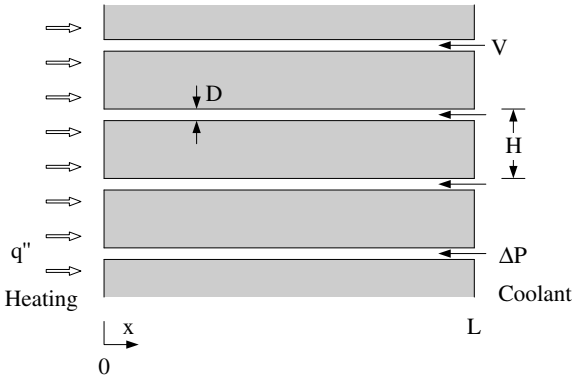

Fig. 1. Two-dimensional parallel channels across a slab with heat flux from one side and forced flow of coolant from the other side.

comes from the left, and the coolant is forced from the right. The solid slab of thickness L and thermal conductivity k is heated from one side with uniform heat flux q''. The other side is insulated. The slab is cooled by a single-phase fluid that flows transversally (along L) against the direction of q''. The flow is driven by a fixed pressure difference ΔP. The fluid flows through parallel slots of width D, one slot for each interval H along the wall. The porosity of the wall ($\phi = D/H$) is fixed.

The lowest temperature (T_{min}) in this flow structure is the fluid inlet temperature. The highest temperature (T_{max}) occurs in hot spots located on the wall surface that receives q''. The objective is to determine the internal spacing D such that the maximum excess temperature ($\Delta T = T_{max} - T_{min}$) is minimum. In other words, we are interested in identifying the internal flow architecture that guarantees the least nonuniform distribution of temperature in the solid. The flow structure is destined to remain imperfect, with cold spots on the surface entered by the fluid, and hot spots on the surface bombarded with q''. The objective in this paper is to identify the least imperfect structure possible.

2. Analytical solution

The analysis that follows is an application of the intersection of asymptotes method [9], which consists of developing analytically the relationship between the global objective (ΔT) and the varying geometry (D) in the two extremes, $D \to 0$ and $D \to \infty$, and using these asymptotes to argue that ΔT can be minimized by selecting D. The optimal D value is located approximately by intersecting the asymptotes.

2.1. The small D limit

Because the porosity is fixed, the limit $D \to 0$ also means $H \to 0$. The L layer can be treated as a fluid saturated porous medium with Darcy flow. The uniform volume averaged velocity V points in the negative x direction,

$$V = \frac{K}{\mu}\frac{\Delta P}{L} \tag{1}$$

The permeability K associated with Poiseuille flow through D-thin fissures is [9]

$$K = \frac{D^2}{12} \tag{2}$$

The temperature distribution across the L is obtained by solving the energy equation

$$-V\frac{dT}{dx} = \alpha\frac{d^2T}{dx^2} \tag{3}$$

subject to the boundary conditions

$$q'' = -k\frac{dT}{dx} \quad \text{at } x = 0 \tag{4}$$

$$T \to T_{min} \quad \text{as } x \to \infty \tag{5}$$

The thermal diffusivity of the saturated porous medium is defined as $\alpha = k/(\rho c_P)_f$, where $(\rho c_P)_f$ is the heat capacity of the fluid, and k is the effective thermal conductivity of the porous medium with the fluid filling its pores. Because the fluid-filled spaces are parallel to the solid parts, and because both are parallel to the direction of heat flow, the effective thermal conductivity is [9]

$$k = \phi k_f + (1-\phi)k_s \tag{6}$$

The solution to Eqs. (3)–(5) is

$$T - T_{min} = \frac{q''\alpha}{kV}\, e^{-Vx/\alpha} \tag{7}$$

and shows that the effect of q'' propagates into the porous structure to a depth x of order α/V. This means that the boundary condition (5) holds when the penetration depth is smaller than the slab thickness

$$\frac{\alpha}{V} < L \tag{8}$$

Finally, from Eq. (7) we find the maximum excess temperature $\Delta T = T_{max} - T_{min}$, which occurs on the $x = 0$ surface

$$\Delta T = \frac{q''\alpha}{kV} \tag{9}$$

After using Eqs. (1) and (2), this result becomes

$$\Delta T = 12\frac{q''\mu L}{D^2 \Delta P (\rho c_P)_f} \tag{10}$$

The first conclusion then is that the maximum excess temperature ΔT increases as $D \to 0$. We are interested in smaller ΔTs, and because of this we turn our attention to how ΔT depends on D in the opposite limit.

2.2. The large D limit

Consider now a situation in which D (or $H = D/\phi$) is sufficiently large that the coolant flows through the channels without experiencing a significant rise in temperature. In this limit, the dominant thermal resistance between the surface with imposed heat flux q'' and the channel surface (the heat sink) is due to heat conduction in square chunks of solid of dimension $H/2$. One such element is shown in Fig. 2. The left side of the square is heated with the flux q'', the top side is isothermal at T_{min}, and the bottom and right sides are adiabatic. The square shape of the domain is not assumed. It follows from the energy equation for steady conduction in a rectangular domain:

$$\frac{\partial^2 T}{\partial x^2} + \frac{\partial^2 T}{\partial y^2} = 0 \tag{11}$$

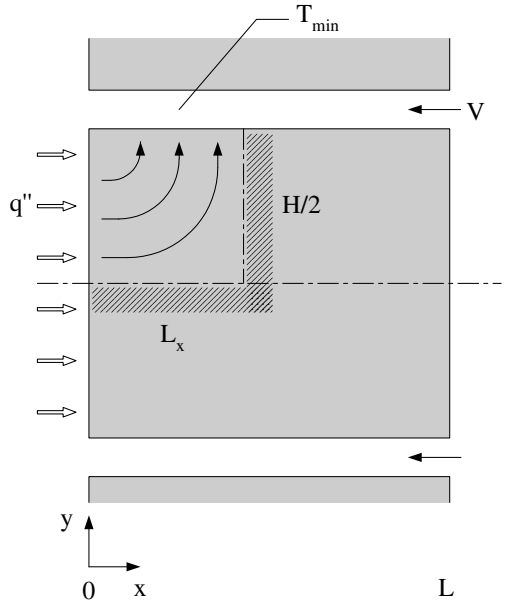

Fig. 2. The 'square' pattern of heat conduction in the large-D limit.

which requires $\Delta T/L_x^2 \sim \Delta T/(H/2)^2$, or that the path of heat conduction in the x direction (L_x, Fig. 2) must have the same length scale as the path in the y direction,

$$L_x \sim \frac{H}{2} \tag{12}$$

The conservation of heat current through the $L_x \times (H/2)$ element requires

$$q''\frac{H}{2} \sim k_s \frac{H}{2}\frac{\Delta T_x}{L_x} \sim k_s L_x \frac{\Delta T_y}{H/2} \tag{13}$$

These relations can be used to estimate the overall temperature difference scale

$$\Delta T \sim \Delta T_x + \Delta T_y \sim \frac{q''}{k_s}\left(L_x + \frac{H^2}{4L_x}\right) \tag{14}$$

which in view of Eq. (12) becomes

$$\Delta T \sim \frac{q''H}{k_s} \sim \frac{q''D}{k_s\phi} \tag{15}$$

This result is valid when the square element $L_x \times (H/2)$ is present, i.e. when the spacing $H/2$ is smaller than the slab thickness,

$$\frac{H}{2} < L \tag{16}$$

The conclusion drawn from Eq. (15) is that in the large D limit the ΔT scale increases as D increases.

2.3. The intersection of asymptotes

Put together, Eqs. (10) and (15) indicate that because ΔT increases in both extremes, it must be minimum at an intermediate D (or ϕH) value, which can be found approximately by intersecting the asymptotes. The result is

Table 1
The values of the group $B\phi^2 k_f/k_s > 1$ for the cases used in the study

B	$\phi = 0.1$			$\phi = 0.2$		
	$k_s/k_f = 10$	30	100	10	30	100
10^6	10^3	3.3×10^2	10^2	4×10^3	1.3×10^3	4×10^2
10^7	10^4	3.3×10^3	10^3	4×10^4	1.3×10^4	4×10^3
10^8	10^5	3.3×10^4	10^4	4×10^5	1.3×10^5	4×10^4

$$\frac{H_{opt}}{L} \cong (12)^{1/3}\phi^{-2/3}B^{-1/3}\left(\frac{k_s}{k_f}\right)^{1/3} \tag{17}$$

where B is the dimensionless pressure drop (or Be [9])

$$B = \frac{\Delta P \cdot L^2}{\alpha_f \mu} \tag{18}$$

and $\alpha_f = k_f/(\rho c_P)_f$. The corresponding minimum ΔT is obtained by substituting H_{opt} into Eq. (15)

$$\Delta T_{min} \cong (12)^{1/3}\frac{q''}{k_s}L\phi^{-2/3}B^{-1/3}\left(\frac{k_s}{k_f}\right)^{1/3} \tag{19}$$

In the course of developing these results we made two assumptions, Eqs. (8) and (16). By using the optimal spacing (17), we find that Eqs. (8) and (16) require, respectively

$$(12)^{-1/3}\phi^{2/3}B^{1/3}\left(\frac{k_s}{k_f}\right)^{-1/3}\frac{1}{1-\phi(1-k_f/k_s)} > 1 \tag{20}$$

$$\left(\frac{2}{3}\right)^{1/3}\phi^{2/3}B^{1/3}\left(\frac{k_s}{k_f}\right)^{-1/3} > 1 \tag{21}$$

In other words, conditions (8) and (16) are essentially the same, and are valid when the group $B\phi^2 k_f/k_s$ is greater than 1. Table 1 shows that this condition is met by the cases studied numerically in this article.

In summary, the best parallel-channels structure for suppressing the hot spots that form on the q'' surface of the slab has the spacings shown in Eq. (17). The minimized hot spot temperature ΔT_{min} decreases further by increasing the applied pressure difference (B), and by making the channel-to-channel spacings smaller.

3. Numerical results

The analytical trends were investigated further by means of numerical simulation and optimization of the heat and fluid flow system of Fig. 1. Because the geometry is periodic in the H direction, it is sufficient to compute the flow and temperature patterns in the elemental volume contained between planes a–a′ and b–b′ in Fig. 3. As shown in the lower part of Fig. 3, the two-dimensional conduction through the solid part is conjugate with convection along the half-channel. The flow system is steady. The flow through the channel is not assumed fully developed: this flow is developing as a result of the pressure difference (ΔP) maintained between the two ends of the channel. The flow rate through one channel is one of the results of the numerical simulation of the heat and fluid flow fields.

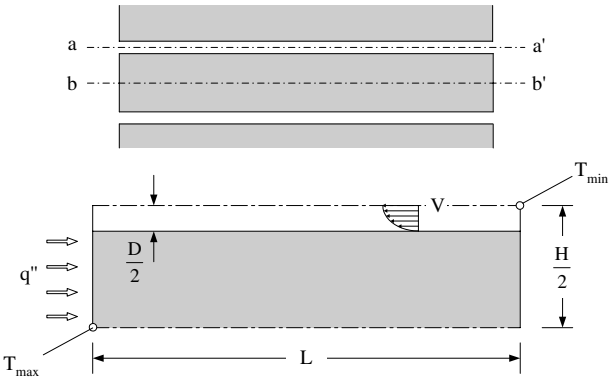

Fig. 3. Elemental fluid–solid volume selected for numerical simulation.

The numerical work consisted of three phases. First, we made sure that the numerical results for each assumed case (assumed D, and fixed external parameters, e.g., ΔP, L, ϕ, q'', material properties) are sufficiently well converged. Second, we conducted several simulations by varying the D value while holding the parameters fixed. We did this in order to identify the optimal configuration (D) in which ΔT is minimal. Third, we correlated the optimized numerical results in the manner indicated by the analytical solution (Eqs. (17) and (19)). This final phase was also an opportunity to verify the analytical results and to describe more accurately their domain of validity.

The computational heat and fluid flow technique was provided by a commercial software [10]. This software provides non-structural grids for a given geometry. Grid fineness was determined using a procedure similar to the accuracy test. We increased the number of elements in steps of 100 beginning with 500. The number of elements is chosen when the criterion ε is less than 0.5%

$$\frac{T_i - T_{i-1}}{T_{i-1}} < \varepsilon \tag{22}$$

In this equation, T_i is a certain spot temperature calculated for ith case (in case no. 1 there were 500 elements, in case no. 2 there were 600 elements, etc.). When using $B = 10^6$, $q'' = 10^5\ W/m^2$, $\frac{H}{L} = 0.5$, $L = 1$ m, $\phi = 0.2$ for water as coolant and 304 stainless steel as solid, numbers of elements greater than 1100 are needed to satisfy Eq. (22). However, for the sake of accuracy, we used more than 2000 elements. One feature of this computational package is that all the physical properties and dimensions of the flow system must be specified in dimensional terms. Consequently, we built the numerical work as a sequence of assumed physical cases, as shown in Table 2. For each case, we specified a set of dimensions and material properties, which also mean that B, ϕ and k_s/k_f are specified. The cases selected for numerical study test the sensitivity of these results in several directions: fluid–solid pairs, cooling intensity (B), porosity (ϕ), etc.

Fig. 4 is an illustration of the temperature field simulated for case 10 in three configurations, $H/L = 0.20$, 0.31 and 0.68. This sequence corresponds to three of the points

Table 2
Cases simulated and optimized numerically ($k_f = 0.613$ W/m K, $q'' = 100$ kW/m^2, $L = 0.01$ m)

Case	$\frac{k_s}{k_f}$	ϕ	ΔPL^2 [Pa m^2]	B
1	10	0.1	1.254×10^{-4}	10^6
2	10	0.1	1.254×10^{-3}	10^7
3	10	0.1	1.254×10^{-2}	10^8
4	30	0.1	1.254×10^{-4}	10^6
5	30	0.1	1.254×10^{-3}	10^7
6	30	0.1	1.254×10^{-2}	10^8
7	100	0.1	1.254×10^{-4}	10^6
8	100	0.1	1.254×10^{-3}	10^7
9	100	0.1	1.254×10^{-2}	10^8
10	10	0.2	1.254×10^{-4}	10^6
11	10	0.2	1.254×10^{-3}	10^7
12	10	0.2	1.254×10^{-2}	10^8
13	30	0.2	1.254×10^{-4}	10^6
14	30	0.2	1.254×10^{-3}	10^7
15	30	0.2	1.254×10^{-2}	10^8
16	100	0.2	1.254×10^{-4}	10^6
17	100	0.2	1.254×10^{-3}	10^7
18	100	0.2	1.254×10^{-2}	10^8

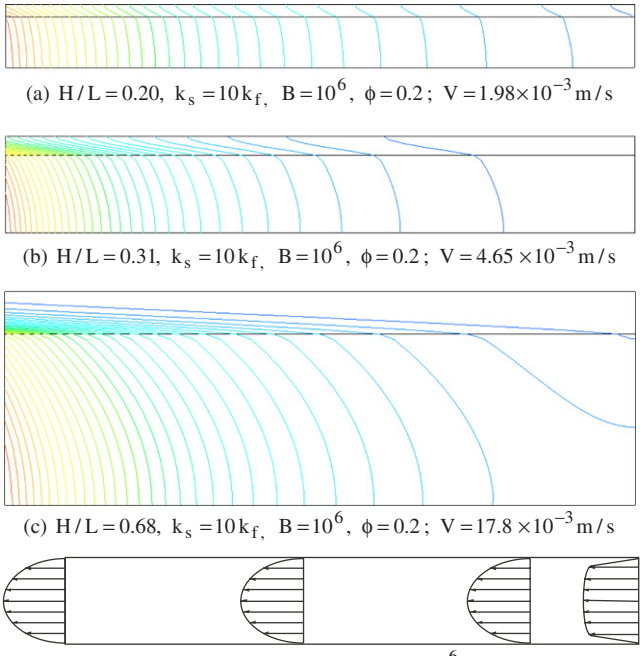

(a) H/L = 0.20, $k_s = 10k_f$, $B = 10^6$, $\phi = 0.2$; V = 1.98×10^{-3} m/s

(b) H/L = 0.31, $k_s = 10k_f$, $B = 10^6$, $\phi = 0.2$; V = 4.65×10^{-3} m/s

(c) H/L = 0.68, $k_s = 10k_f$, $B = 10^6$, $\phi = 0.2$; V = 17.8×10^{-3} m/s

(d) Example of velocity profile development ($B = 10^6$, H/L = 0.68, $\phi = 2.0$)

Fig. 4. Samples of temperature and velocity results.

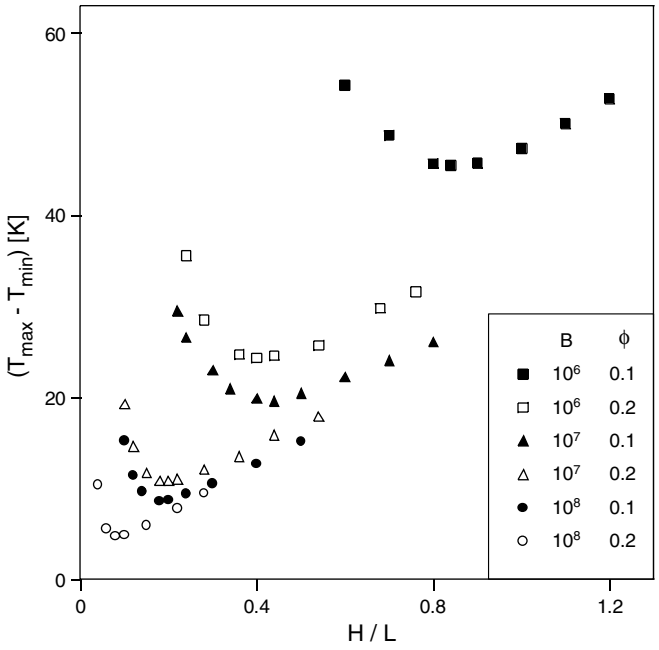

Fig. 5. The optimization of D (or H) for several of the cases listed in Table 2.

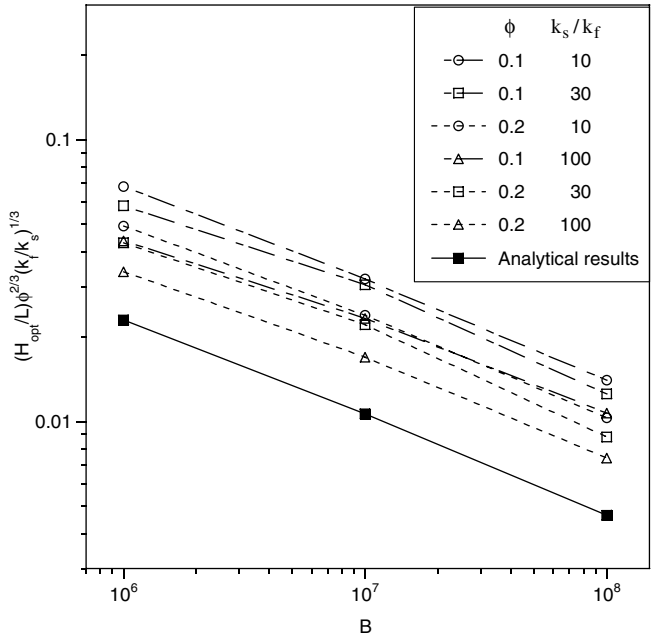

Fig. 6. Correlation of numerical and analytical results for the optimal channel-to-channel spacing.

shown on the $B = 10^6$ and $\phi = 0.2$ curve in Fig. 5. We generated such sequences by varying D (or H) until the overall temperature difference across the elemental volume ($\Delta T = T_{max} - T_{min}$) reached its minimum value. Fig. 5 shows that the ΔT minimum is well defined, and that its position on the ΔT–H/L map depends on B. The optimized H/L and the minimized ΔT decrease as B increases.

After performing this geometry optimization work for all the cases listed in Table 1, we collected the results [H_{opt}/L, ΔT_{min}] and projected them in dimensionless terms as shown in Figs. 6 and 7. For the optimal channel-to-channel spacing, we used the group $(H_{opt}/L)\ \phi^{2/3}\ (k_f/k_s)^{1/3}$ on the ordinate, as suggested by Eq. (17). This group is expected to vary as $B^{-1/3}$, and the numerical results confirm this trend.

For the minimized overall ΔT, we used the group $\Delta T_{min} k_s/(q'' L)\phi^{2/3}(k_f/k_s)^{1/3}$ on the ordinate. This dimensionless group is suggested by Eq. (19), according to which the group should be proportional to $B^{-1/3}$. The optimized numerical cases confirm this trend as well.

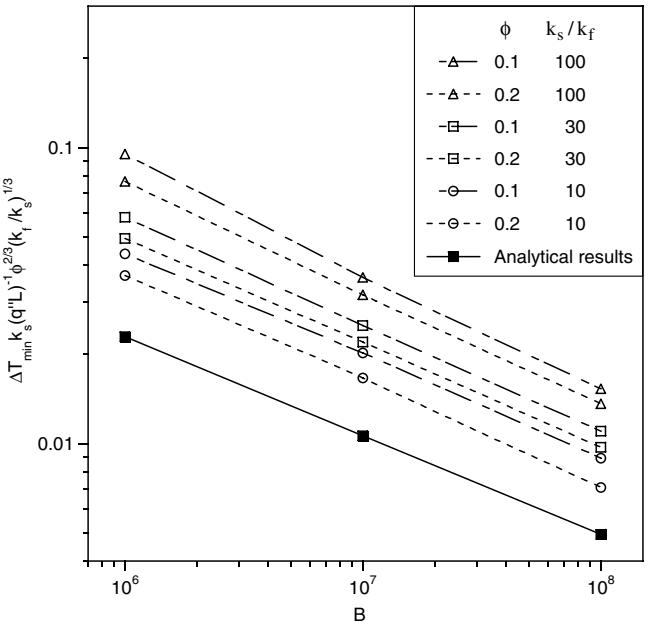

Fig. 7. Correlation of numerical and analytical results for the minimized global temperature difference.

Together Figs. 6 and 7 show that the numerical results validate the analytical formulas. Furthermore, the numerical and analytical results show that in all the optimized configurations the global parameters (ϕ and B) influence in the same way H_{opt}/L and ΔT_{min}. This peculiarity of the optimized configurations can be expressed succinctly as a proportionality between ΔT_{min} and H_{opt}/L, which is obtained by dividing Eq. (19) by Eq. (17):

$$\frac{\Delta T_{min}}{H_{opt}/L} \cong \frac{q''L}{k_s} \tag{23}$$

Note that this agrees with Eq. (15), because each of the optimized configurations represented by Eq. (23) finds itself at the intersection of Eqs. (15) and (10).

4. Parallel round channels across a slab

An alternate configuration for fighting the heat flux by forcing coolant from the opposite side is shown in Fig. 8. The coolant flows through channels with round cross-section (diameter D, length L). Assume that the channels are arranged in a square pattern with the distance H between tube centers. Because of periodicity in the H direction, it is sufficient to optimize the configuration of a single volume element with the volume $H \times H \times L$, which has a single channel centered on its long axis of symmetry.

The analysis of this volume element is completely analogous to what we presented in Section 2 for the two-dimensional elemental volume of Fig. 3. In this section we highlight the differences. In place of Eqs. (2), (10) and (15) now we have [9]

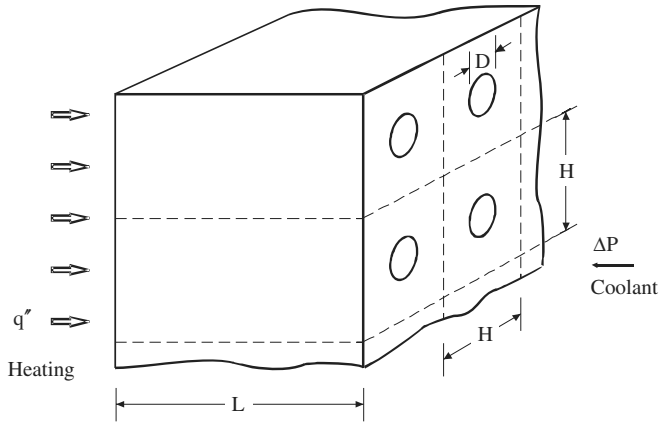

Fig. 8. Round channels across a slab with heat flux from one side and forced flow from the other side.

$$K = \frac{D^2}{g}, \quad \phi = \frac{\pi D^2}{4H^2} \tag{24}$$

$$\Delta T \cong g\frac{q''\mu L}{D^2 \Delta P (\rho c_P)_f} \tag{25}$$

$$\Delta T \cong \frac{q''}{k_s} \cdot \frac{3H}{4} \tag{26}$$

where $g = 32/\phi$. The intersection of the asymptotes (25) and (26) yields

$$\frac{H_{opt}}{L} \cong \left(\frac{32}{3}\pi\right)^{1/3} \phi^{-2/3} B^{-1/3} \left(\frac{k_s}{k_f}\right)^{1/3} \tag{27}$$

$$\Delta T_{min} \cong \frac{3}{4}\left(\frac{32}{3}\pi\right)^{1/3} \frac{q''}{k_s} L \phi^{-2/3} B^{-1/3} \left(\frac{k_s}{k_f}\right)^{1/3} \tag{28}$$

Important is the observation that these optimization results agree within a factor of order 1 with the corresponding results for two-dimensional channels (Section 2). This

Table 3
Cases simulated and optimized numerically ($k_f = 0.613$ W/m K, $q'' = 100$ kW/m^2, $L = 0.01$ m)

Case	$\frac{k_s}{k_f}$	ϕ	$\Delta P L^2$ [Pa m^2]	B
1	10	0.05	1.254×10^{-4}	10^6
2	10	0.05	1.254×10^{-3}	10^7
3	10	0.05	1.254×10^{-2}	10^8
4	30	0.05	1.254×10^{-4}	10^6
5	30	0.05	1.254×10^{-3}	10^7
6	30	0.05	1.254×10^{-2}	10^8
7	100	0.05	1.254×10^{-4}	10^6
8	100	0.05	1.254×10^{-3}	10^7
9	100	0.05	1.254×10^{-2}	10^8
10	10	0.1	1.254×10^{-4}	10^6
11	10	0.1	1.254×10^{-3}	10^7
12	10	0.1	1.254×10^{-2}	10^8
13	30	0.1	1.254×10^{-4}	10^6
14	30	0.1	1.254×10^{-3}	10^7
15	30	0.1	1.254×10^{-2}	10^8
16	100	0.1	1.254×10^{-4}	10^6
17	100	0.1	1.254×10^{-3}	10^7
18	100	0.1	1.254×10^{-2}	10^8

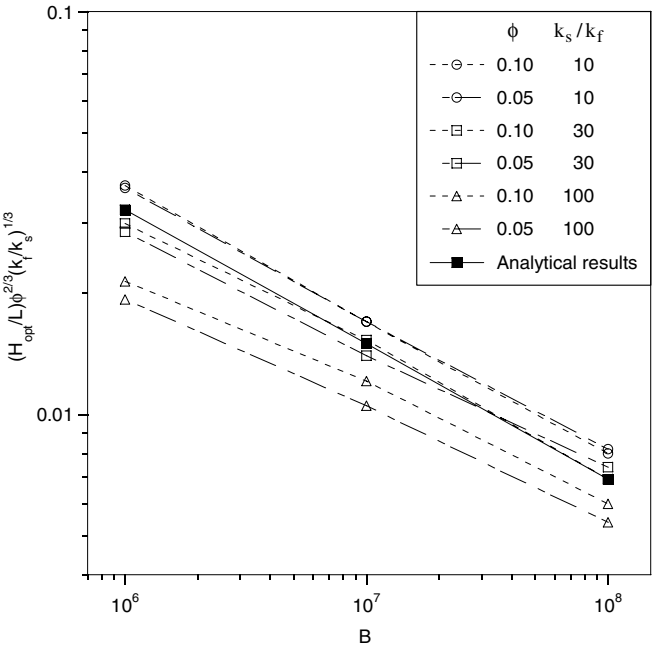

Fig. 9. The optimal channel-to-channel spacings for the configuration of Fig. 8.

means that the scaling laws (17), (19), (27) and (28) are robust. They depend on global parameters of the structure (ϕ, B, L, q'', k_s, k_f), not on the cross-sectional shapes of the channels through which the coolant is forced to flow. Robustness is a precious quality in rules that are used for sizing complex flow architectures.

We tested numerically the validity of Eqs. (27) and (28) by using the same procedure as in Section 3. Table 3 shows

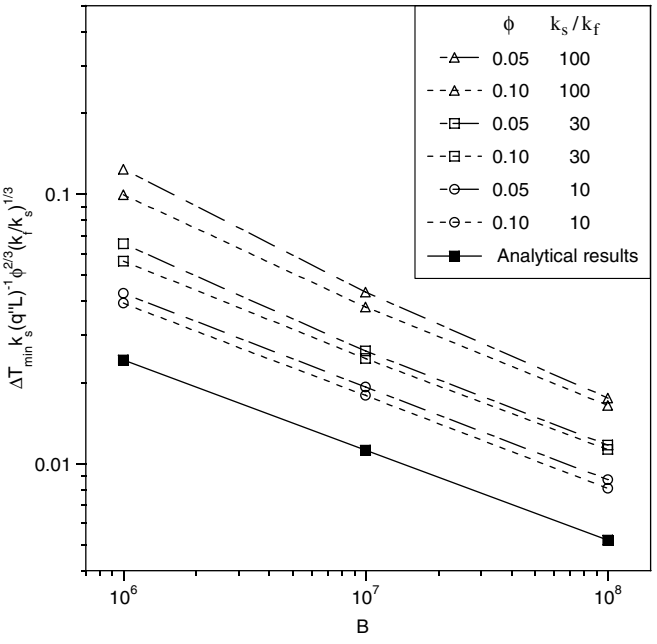

Fig. 10. The minimized global temperature difference for the configuration of Fig. 8.

the properties for the cases considered in this study. With reference to Fig. 8, we simulated numerically the conjugate heat transfer in an elemental volume $H \times H \times L$ with developing laminar flow through a central duct of diameter D. For each assumed elemental configuration, we estimated the maximum temperature T_{max}, which forms in the corners of the $H \times H$ square in the exit plane. The lowest temperature (T_{min}) is the inlet temperature of the coolant. We searched through many configurations with differing H values until we found the configuration with the smallest $\Delta T = T_{max} - T_{min}$. The results for H_{opt}/L and ΔT_{min} are reported in Figs. 9 and 10. The agreement between these numerical results and predictions based in Eqs. (27) and (28) is adequate (within a factor of order 1). This level of agreement between numerical testing and the intersection of asymptotes method is the same as in Figs. 6 and 7. This finding adds to the robustness of the scaling trends developed analytically.

5. Discussion

In this paper we have taken a fundamental look at the proposal to vascularize a wall such that the coolant pushed in from one side is effective in fighting off the intense heating that strikes the slab from the other side. The fundamental conclusion of this investigation is that it is possible to select the internal configuration of the flow system (the vascularization) such that the solid body is protected most effectively against overheating.

The main results of this work are the formulas that indicate the optimal configuration for vascularization [Eqs. (17) and (27)] and the minimized temperature nonuniformity of the flow system [Eqs. (19) and (28)]. These results have been validated based on numerical simulations of heat and fluid flow in two-dimensional and three-dimensional geometries (Figs. 1 and 8). The results teach the designer how to size the internal vasculature, and what to expect as performance when the heat flux and the pressure difference are specified.

Important is also the robustness of these results: Eq. (17) looks like Eq. (27) and Eq. (19) looks like Eq. (28). The numerical simulation and optimization work showed that the $B^{-1/3}$ trend anticipated by these formulas is correct, but that the trends with respect to changes in ϕ and k_f/k_s are correct only qualitatively. In this concluding section we take a closer look at the ϕ and k_f/k_s effects, in order to describe more accurately the robustness of the results.

Because of Eqs. (17), (19), (27) and (28), we correlated the numerical optimization results by plotting on the ordinates of Figs. 6, 7, 9 and 10 the groups

$$\frac{H_{opt}}{L}\phi^a\left(\frac{k_f}{k_s}\right)^b \qquad \frac{\Delta T_{min} k_s}{q''L}\phi^a\left(\frac{k_f}{k_s}\right)^b$$

The theoretical exponents are $a = 2/3$ and $b = 1/3$. These exponents are not the best, as indicated by the scatter in the numerical data plotted in Figs. 6, 7, 9 and 10.

In the construction of the new Figs. 11–14, we allowed the exponents a and b to vary until all the numerical data collapsed on the respective analytical curve. In this way we discovered the empirical constants (a and b) with which to correlate the numerical and analytical results. These constants are reported in Table 4, and are valid over the parametric domain covered by the cases simulated numerically (Table 2). It is clear that the empirically optimized constants (a and b) are of the same order of magnitude

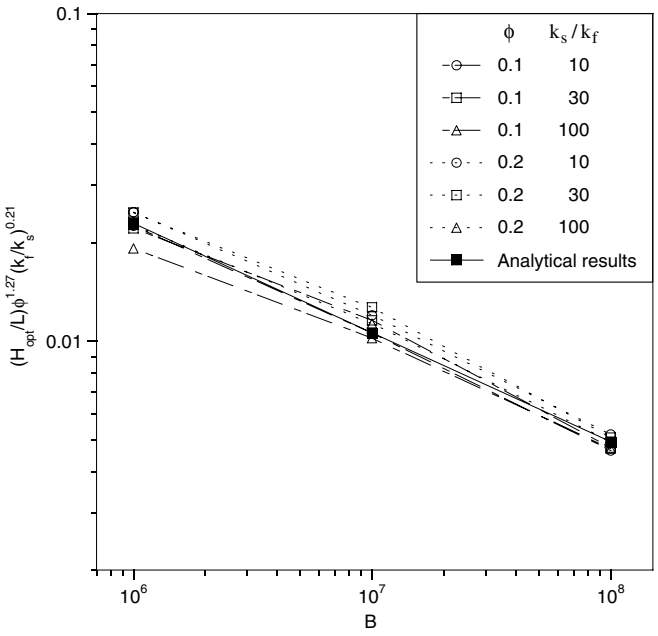

Fig. 11. The data of Fig. 6 replotted by using $\phi^{1.27}(k_f/k_s)^{0.21}$ in the group on the ordinate.

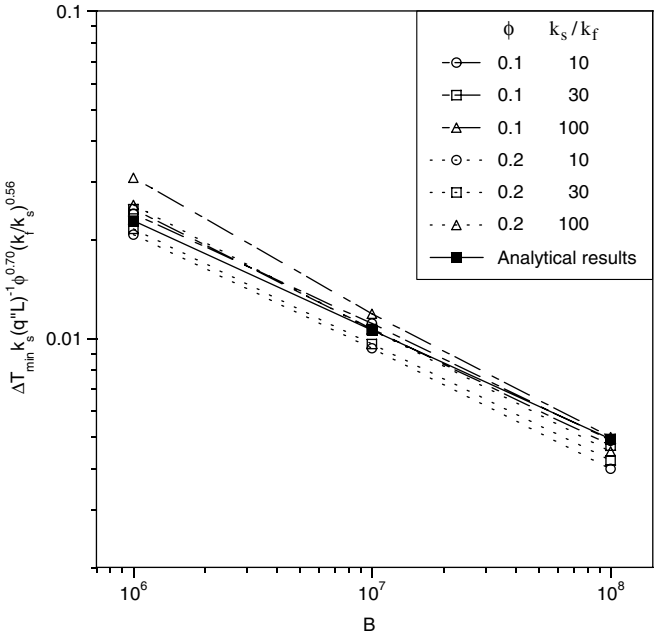

Fig. 12. The data of Fig. 7 replotted by using $\phi^{0.7}(k_f/k_s)^{0.56}$ in the group on the ordinate.

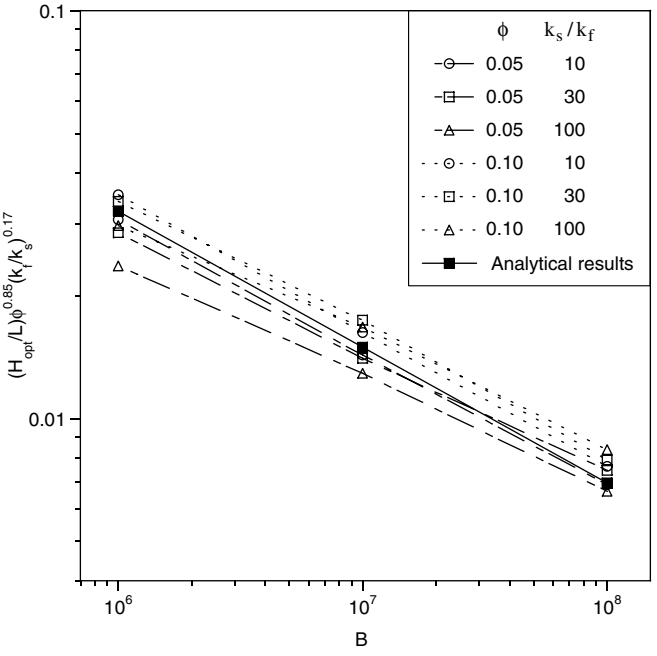

Fig. 13. The data of Fig. 9 replotted by using $\phi^{0.85}(k_f/k_s)^{0.17}$ in the group on the ordinate.

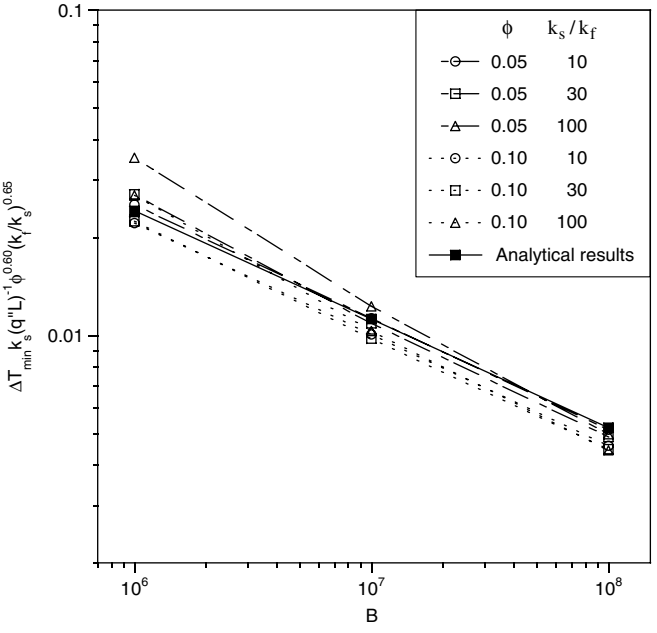

Fig. 14. The data of Fig. 10 replotted by using $\phi^{0.6}(k_f/k_s)^{0.65}$ in the group on the ordinate.

Table 4
Comparison between the optimized exponents (a and b) and the analytical values

	H/L, 2-D Fig. 11	ΔT_{min}, 2-D Fig. 12	H/L, 3-D Fig. 13	ΔT_{min}, 3-D Fig. 14	Analytical results
a	1.27	0.70	0.85	0.60	0.67
b	0.21	0.56	0.17	0.65	0.33

as the theoretical exponents. Once again, this means that Eqs. (17), (18), (27) and (28) are robust, however, for greater accuracy the designer should rely on the empirically fitted correlations displayed in Figs. 11–14.

The fast growing research literature on constructal theory, design and vascularized smart materials was just reviewed in Refs. [11,12].

Acknowledgements

This work was supported by a grant from the Air Force Office of Scientific Research for "Constructal technology for thermal management of aircraft", and by a MURI project on "Microvascular autonomic composites", which is pursued at the University of Illinois at Urbana-Champaign, Duke University and the University of California at Los Angeles.

References

[1] A. Bejan, Advanced Engineering Thermodynamics, second ed., Wiley, New York, 1997.
[2] A.H. Reis, Constructal theory: from engineering to physics, and how flow systems develop shape and structure, Appl. Mech. Rev. 59 (2006) 269–282.
[3] A. Bejan, Shape and Structure, from Engineering to Nature, Cambridge University Press, Cambridge, UK, 2000.
[4] S.R. White, N.R. Sottos, J. Moore, P. Geubelle, M. Kessler, E. Brown, S. Suresh, S. Viswanathan, Autonomic healing of polymer composites, Nature 409 (2001) 794–797.
[5] A. Bejan, S. Lorente, K.-M. Wang, Network of channels for self-healing composite materials, J. Appl. Phys. 100 (2006) 033528.
[6] K.-M. Wang, S. Lorente, A. Bejan, Vascularized networks with two optimized channels sizes, J. Phys. D: Appl. Phys. 39 (2006) 3086–3096.
[7] S.-W. Kim, S. Lorente, A. Bejan, Vascularized materials: tree-shaped flow architectures matched canopy to canopy, J. Appl. Phys. 100 (2006) 063525.
[8] S. Lorente, A. Bejan, Heterogeneous porous media as multiscale structures for maximum flow access, J. Appl. Phys. 100 (2006) 114909.
[9] A. Bejan, Convection Heat Transfer, third ed., Wiley, Hoboken, 2004.
[10] Starccm+ (Version 1.04) basics, CD-adapoco Company.
[11] A. Bejan, S. Lorente, Constructal theory of generation of configuration in nature and engineering, J. Appl. Phys. 100 (2006) 041301.
[12] A. Bejan, Advanced Engineering Thermodynamics, third ed., Wiley, Hoboken, 2006.